

Supporting Information for:

Sizing single trapped nanoparticles with interferometric scattering fluctuations

Abhijit A Lavania and William B Carpenter

Contents

| | |
|--|----|
| Note S1: Derivation of analytical contrast autocorrelation function | 2 |
| Note S2: ISABEL simulation details | 3 |
| Note S3: Characterization of ABEL Cell Depth | 7 |
| Table S1: Universal simulation parameters | 8 |
| Table S2: Particle-specific simulation parameters | 8 |
| Supplementary Figures | 9 |
| Supplementary References | 17 |

Note S1: Derivation of analytical contrast autocorrelation function

Consider a Rayleigh scatterer diffusing above a reflective interface according to an isotropic diffusion coefficient D and illuminated by a plane wave $E\cos(kz+\omega t)$. For simplicity, we assume monochromatic illumination and infinite coherence length. Because of the optical delay between the reflected and scattered fields, the interferometric scattering contrast can be described as:

$$c(t) = \frac{2|E_s|\cos[2kz(t)]}{|E_r|} \propto \cos[2kz(t)] \quad (\text{S1})$$

Therefore the time autocorrelation function of the contrast can be written down as

$$ACF(\tau) = \frac{\langle c(t)c(t+\tau) \rangle}{\langle c^2(t) \rangle} \quad (\text{S2a})$$

$$= \frac{\langle \cos[2kz(t)] \cos[2kz(t+\tau)] \rangle}{\langle \cos^2[2kz(t)] \rangle} \quad (\text{S2b})$$

$$= \frac{\langle \cos[2kz(t)] \cos[2k(z+\Delta z(\tau))] \rangle}{\langle \cos^2[2kz(t)] \rangle} \quad (\text{S2c})$$

$$= \langle \cos(2k\Delta z(\tau)) \rangle \quad (\text{S2d})$$

Where the final line arises from simplifying by trigonometric identities, including noting that $\langle \sin 4kz \rangle = 0$. To evaluate the ACF, we consider the displacement probability distribution for 1-dimensional Brownian motion:

$$P(\Delta z|\tau) \sim \exp\left(-\frac{\Delta z^2}{4D\tau}\right) \quad (\text{S3})$$

To simplify evaluation, we introduce dimensionless parameters:

$$\tilde{\Delta z} = 2k\Delta z(\tau) \quad (\text{S4})$$

$$\tilde{\sigma}^2 = 8k^2D\tau \quad (\text{S5})$$

$$P(\tilde{\Delta z}|\tau) = \exp\left(-\frac{\tilde{\Delta z}^2}{2\tilde{\sigma}^2}\right) \quad (\text{S6})$$

This leaves us to evaluate $ACF(t) = \langle \cos(Z) \rangle$ Where Z is a random variable drawn from $P(\tilde{\Delta z}|\tau)$:

Taylor series expansion: $\langle \cos(Z) \rangle = \left\langle \sum_{k=0}^{\infty} (-1)^k \frac{1}{(2k)!} (Z)^{2k} \right\rangle \quad (\text{S7a})$

Commuting sums: $= \sum_{k=0}^{\infty} (-1)^k \frac{1}{(2k)!} \langle (Z)^{2k} \rangle \quad (\text{S7b})$

Even moments of normal distribution: $= \sum_{k=0}^{\infty} (-1)^k \frac{1}{(2k)!} \tilde{\sigma}^{2k} (2k-1)!! \quad (\text{S7c})$

$= \tilde{\sigma}^{2k} (2k-1)!!$
 $= \tilde{\sigma}^{2k} (2k-1)(2k-3) \dots 1$

$$\begin{aligned}
& \frac{(2k-1)!!}{(2k)!} \\
&= \frac{(2k-1)(2k-3)\dots 1}{(2k)(2k-1)\dots 1} \\
&= \frac{1}{2^k k!}
\end{aligned}
\quad = \sum_{k=0}^{\infty} (-1)^k \frac{1}{2^k k!} \tilde{\sigma}^{2k} \tag{S7d}$$

$$= \sum_{k=0}^{\infty} \frac{\left(-\frac{\tilde{\sigma}^2}{2}\right)^k}{k!} = \exp\left(-\frac{\tilde{\sigma}^2}{2}\right) \tag{S7e}$$

$$= \exp(-4k^2 D\tau) \tag{S7f}$$

Note S2: ISABEL simulation details

Confinement effects on diffusion

The confinement effects on diffusion arise due to symmetry breaking near a wall and the attenuation of the long-range collective forces from the solvent acting on the particle. The relative diffusion attenuation is well-approximated in terms of the ratio a/z of the particle radius a and distance z from a wall:¹

$$\lambda_{\perp} = \frac{6-10\left(\frac{a}{z}\right)+4\left(\frac{a}{z}\right)^2}{6-3\left(\frac{a}{z}\right)-\left(\frac{a}{z}\right)^2} \tag{S8}$$

$$\lambda_{\parallel}^{-1} = 1 - \frac{8}{15} \ln\left(1 - \frac{a}{z}\right) + 0.029\left(\frac{a}{z}\right) + 0.04973\left(\frac{a}{z}\right)^2 - 0.1249\left(\frac{a}{z}\right)^3 \tag{S9}$$

where λ_{\perp} corresponds to the diffusion attenuation perpendicular to the wall (i.e. in z), and λ_{\parallel} corresponds to the direction parallel to the wall (x and y).

To account for the attenuations from two walls (λ_{w1} and λ_{w2}) separated by a height h , we apply the effect of each independently, known as the linear superposition approximation:²

$$\lambda_{2w}(z) = \lambda_{w1}(z) + \lambda_{w2}(h-z) - 1 \tag{S10}$$

Therefore for the ISABEL geometry, $D_z(z) = \lambda_{\perp,2w}(z)D_0$ and $D_{xy}(z) = \lambda_{\parallel,2w}(z)D_0$. The z -dependent D_z and D_{xy} values for a 100 nm bead in a 690 nm channel are shown below in Fig. S6, and the ACF accounting for confined diffusion of a model 100 nm particle is shown in Fig. S2.

Optical forces

In addition to confinement, we incorporated the effect of optical forces on the particle. For each simulated particle, we could attribute scattering and absorption cross sections σ_{scat} and σ_{abs} at 808 nm as determined by our past measurements.³ For example, the 100 nm polystyrene beads exhibited an average $\sigma_{\text{scat}} = 36 \text{ nm}^2$ and $\sigma_{\text{abs}} = 0 \text{ nm}^2$, whereas a 50 nm Au bead exhibits $\sigma_{\text{scat}} = 52 \text{ nm}^2$ and $\sigma_{\text{abs}} = 52 \text{ nm}^2$ on average. To account for the range of σ_{scat} values over a range of particle diameters d_i , we approximate a scaled scattering cross-section $\sigma_{\text{scat},i}$ for an individual particle:

$$\sigma_{\text{scat},i} = \sigma_{\text{scat,mean}} (d_i/d_{\text{mean}})^6 \quad (\text{S11})$$

in accordance with the Rayleigh regime for scaling of scattering cross section. Mean scattering cross sections for each class of particles are listed in Table S2. Additionally, our scattering illumination beam was determined to have a power of 20 mW for most samples (7 mW for 50 nm Au NPs and 130 nm polystyrene NPs) and a $1/e^2$ radius of 790 nm, leading to a peak intensity $I_{\text{pk}} 510 \text{ kW/cm}^2$ and average power 16 kW/cm^2 over the Knight's Tour pattern. From these quantities, we could calculate the scattering force acting on our particle:⁴

$$\mathbf{F}_{\text{scat}}(r) = \frac{n_m \sigma_{\text{ext}}}{c} \mathbf{S}(r) = \frac{n_m \sigma_{\text{ext}}}{c} I(r) \hat{\mathbf{z}} \quad (\text{S12})$$

Where $\sigma_{\text{ext}} = \sigma_{\text{scat}} + \sigma_{\text{abs}}$ is the extinction cross section of the particle, n_m is the refractive index of the medium (Table S1), and \mathbf{S} is the Poynting vector of the beam. For a 100 nm PS bead, $\mathbf{F}_{\text{scat}} = 1.62 \text{ fN}$ at the center of the beam.

Gradient forces were determined according to the following expression:⁴

$$\mathbf{F}_{\text{grad}}(r) = \frac{\alpha'_p}{2cn_m} \nabla I(r) = \frac{\alpha'_p}{2cn_m} \nabla \left[I_0 \exp\left(-\frac{2r^2}{w_0^2}\right) \right] \quad (\text{S13a})$$

$$= \frac{-2I_0 \alpha'_p}{w_0^2 c n_m} r \exp\left(-\frac{2r^2}{w_0^2}\right) = -k_r r \exp\left(-\frac{2r^2}{w_0^2}\right) \quad (\text{S13b})$$

where I_0 is the incident beam's peak intensity, w_0 is the beam waist, c is the vacuum speed of light, and k_r is the radial spring constant. α'_p is the real part of the particle's polarizability, related to σ_{scat} by:⁵

$$|\alpha'_p|^2 = \frac{3}{8\pi^2} \sigma_{\text{scat}} \lambda_m^4 \quad (\text{S14})$$

where $\lambda_m = \lambda_0/n_m$ is the field's wavelength in the medium. The maximum lateral gradient force $\mathbf{F}_{\text{grad}}(r)$ for a 100nm polystyrene bead was determined to be 7.9 fN. Finally, the gradient force in the z dimension was determined making the harmonic approximation such that:

$$\mathbf{F}_{\text{grad}}(z) = k_z (z - z_0) = k_r \frac{\lambda_m^2}{(\pi w_0)^2} (z - z_0) \quad (\text{S15})$$

where z_0 is the focal position of the Gaussian beam. For a 100nm polystyrene bead, the maximal axial gradient force $\mathbf{F}_{\text{grad}}(z)$ was 0.6 fN.

In the simulation, \mathbf{F}_{scat} and \mathbf{F}_{grad} acting on the particle were calculated at each time step and used to calculate the three-dimensional placements of the particle as part of the third terms in Eq. 6-8 in the main text. Despite being comparable in magnitude to the scattering force, gradient forces were found to have negligible influence on the particle's contrast ACF (Fig. S7c) due to their isotropic orientation. The gradient force in z was smallest: on average 0.8 aN with a maximum value of 0.6 fN. However, the scattering force was unidirectional, resulting in an average force of +0.2 fN and a bias where particles preferentially explored higher regions nearer the top wall. By biasing particles closer to the top wall, they experience an even slower $\langle D_z \rangle$ than expected due to confinement alone. The corresponding forces for 50nm Au nanoparticles were: axial scattering (average +0.2 fN, maximum 1.9 fN) and lateral gradient forces (average -7 aN, maximum 3.5 fN).

Interferometric scattering contrast model

To ensure efficient determination of the interferometric scattering contrast at each point, we implemented a contrast lookup table, which determined normalized interferometric scattering contrast $c(z, r)$ as a function of particle height z and distance r from the beam center r_0 .

The model is based on the scattering of circularly polarized light from a dipole above a glass surface.⁶⁻

⁸ Consider a Rayleigh scatterer illuminated by a Gaussian beam described by the equation:

$$E_i(r, z) = \frac{w_0}{w_z} e^{-\frac{(r-r_0)^2}{w_z^2}} \exp(-ik(z-z_0) + k(z-z_0)^2 R_z^{-1} - \tan^{-1}\left(\frac{z-z_0}{z_r}\right)) \quad (\text{S16})$$

Where $r = (x^2 + y^2)^{1/2}$ is the distance from the beam's optical axis at r_0 , w_0 is the focal waist, w_z is the waist a distance z above the focus, and z_0 is the focal height of the beam with respect to the surface, which we took to be the midpoint between the two walls at $z = 345$ nm. The z -dependent radius of curvature R_z and Guoy phase appear in the penultimate and final terms in parentheses, respectively.

The reflected Gaussian beam is given by

$$E_r(r, z) = -r_q \frac{w_0}{w_z} e^{-\frac{(r-r_0)^2}{w_z^2}} \exp(-ik(z-z_0) + k(z-z_0)^2 R_z^{-1} - \tan^{-1}\left(\frac{z-z_0}{z_r}\right)) \quad (\text{S17})$$

Where r_q is the depolarized Fresnel reflectivity coefficient at the quartz-water interface. The negative sign prefactor indicates the reversal of propagation direction of the reflected beam. We can treat the reflection as from one surface (even though we have two surfaces in the trap) since it can be shown that the effect of two flat surfaces is a net reflected field that is merely a scaled version of the first reflection. As well, since the two surfaces are within the Rayleigh length of $\sim 2\mu\text{m}$, there is no significant defocus between the two reflections of the incident Gaussian beam.

Upon illumination, the Rayleigh scatter emits an electric field according to a dipole pattern with an orientation $\hat{\mu}$ of the emitter dipole induced by the incident field. The emission from this induced

dipole can then be modeled with a vectorial imaging model.^{7,8} For a point-like particle illuminated by circularly polarized light, the dipole emission pattern appears radially polarized in the transverse direction, such that we can describe it as

$$\hat{\boldsymbol{\mu}} = \begin{bmatrix} \mu_x \\ \mu_y \\ \mu_z \end{bmatrix} = \frac{|\boldsymbol{\mu}|}{\sqrt{2}} \begin{bmatrix} 1 \\ i \\ 0 \end{bmatrix} \quad (\text{S18})$$

At the sample, the *s*- and *p*-polarized components of the radiated electric field are:⁷

$$E_s(\theta_2, \phi) = t_s \frac{n_1 \cos(\theta_1)}{n_2 \cos(\theta_2)} [\mu_y \cos(\phi) - \mu_x \sin(\phi)] \quad (\text{S19})$$

$$E_p(\theta_2, \phi) = t_p \frac{n_1}{n_2} \left[\cos(\theta_1) (\mu_x \cos(\phi) + \mu_y \sin(\phi)) - \mu_z \sin(\theta_1) \frac{n_1 \cos(\theta_1)}{n_2 \cos(\theta_2)} \right] \quad (\text{S20})$$

where θ_1 and θ_2 are polar angles of the emission in quartz and water, respectively and related by Snell's Law, ϕ is the emission's polar angle, n_1 and n_2 are the refractive indices in quartz and water, respectively, and t_s and t_p are the Fresnel transmission coefficients for *s* and *p* polarized light. A diagram of the coordinate system is provided in Fig. S11a.

These fields propagate through the objective to result in back-focal plane field components

$$E_{bfp,x}(\theta_1, \phi) = \frac{1}{\sqrt{\cos(\theta_1)}} [E_p \cos(\phi) - E_s \sin(\phi)] \exp[ik_1 z_0 \cos(\theta_1)] \exp \left[ik_2 z \cos(\theta_2) + \frac{\pi}{2} \right] \quad (\text{S21})$$

$$E_{bfp,y}(\theta_1, \phi) = \frac{1}{\sqrt{\cos(\theta_1)}} [E_s \cos(\phi) + E_p \sin(\phi)] \exp[ik_1 z_0 \cos(\theta_1)] \exp \left[ik_2 z \cos(\theta_2) + \frac{\pi}{2} \right] \quad (\text{S22})$$

Where the first bracketed term corresponds to the coordinate rotation to convert *s*- and *p*-polarizations to *x* and *y*, the first exponential corresponds to the phase delay associated with the beam's focal height, and the second exponential corresponds to the phase delay due to the height of the particle and $\pi/2$ phase delay due to nonresonant scattering. The back-focal-plane field is apertured according to the NA of the objective. A representative back-focal plane intensity $|E_{bfp,x} + E_{bfp,y}|^2$ for a scatterer at $z = 350$ nm is shown in Fig. S11b.

Finally, the dipole emission pattern in the image plane conjugate to the sample plane is the 2D Fourier transform of the back-focal-plane field:

$$\mathbf{E}_{\text{scat}}(x, y) = FT \left\{ \begin{bmatrix} E_{bfp,x}(\theta_1, \phi) \\ E_{bfp,y}(\theta_1, \phi) \end{bmatrix} \right\} \quad (\text{S23})$$

The scattering intensity $|E_{\text{scat},x} + E_{\text{scat},y}|^2$ in the sample plane is shown in Fig. S11c.

With the scattering and reflected fields determined, the interferometric scattering contrast was calculated according to:

$$c = \frac{\sum_{x,y} |E_r(x,y) + E_{\text{scat}}(x,y)|^2 - \sum_{x,y} |E_r(x,y)|^2}{\sum_{x,y} |E_r(x,y)|^2} \quad (\text{S24})$$

where the summations arise from detection on a single-element photoreceiver.

Finally, to assemble the contrast map, we repeated the above Gaussian beam and dipole scattering calculations over a grid of $z \in [0: 10: 690]$ nm and $r \in [0:40:800]$ nm, further interpolated to a grid spacing of 3.45 nm in z and 8 nm in r . The contrast map was then normalized to the value of highest absolute contrast. During a Brownian Dynamics simulation, the particle's z position and distance r from the scanning beam was determined at each time step and matched to the corresponding position to extract its contrast $c(t)$.

Note S3: Characterization of ABEL Cell Depth

To accurately model the hydrodynamic confinement effects felt by each nanoparticle, we required an accurate estimation of the microfluidic cell height. We achieved this by white light interferometry, where the reflected spectrum of a white light source (Leukos Rock 400 supercontinuum) displayed oscillations due to interference between the two surfaces. The illumination geometry is shown in Fig. S3 below.

We measured the reflected spectrum from the trapping region of an ABEL cell with a fiber spectrometer (Ocean Optics), normalized by the reflection of a single quartz surface to retrieve the fringes as a function of wavelength. The interference of two reflections $I_{r,tot}$ can be described by the following equation:

$$I_{r,tot}(\tilde{\nu}) = \cos(4\pi n \tilde{\nu} h) \quad (\text{S25})$$

Where $\tilde{\nu}$ is the spectroscopic wavenumber, n is the index of refraction in the gap, and h is the distance between the two walls. We measured the reflected spectrum with an air gap such that $n=1$. As shown in Fig. S4, the ABEL cell used for the bead standards exhibited $h = 690$ nm gap, whereas the cell used to trap carboxysomes showed a height $h = 1260$ nm.

Table S1: Universal simulation parameters

| Parameter | Value | Experimental Value (method) |
|---------------------------------|-----------------------|---|
| Temperature T | 19.0 °C | 18.7-19.2 °C (thermistor on microfluidic cell) |
| Viscosity η | 1.03 mPa·s | 1.03 mPa·s (tabulated $\eta_{\text{H}_2\text{O}}$ at 19 °C with Jones-Dole parameters for NaCl at 20 °C) ⁹ |
| Beam Wavelength λ | 808 nm | 808 nm (fiber spectrometer) |
| Medium refractive index n | 1.33 | 1.33 (tabulated) |
| Beam Waist w_0 | 790 nm | 790 nm (imaged beam reflection) |
| Beam axial focal position z_f | 345 nm | Taken as midpoint of cell |
| Feedback gain g | 2.28 V/ μm | 2.28 V/ μm (multimeter readout at 1 μm displacement of fixed bead) |

Table S2: Particle-specific simulation parameters

| Particle | Electrokinetic Mobility μ ($\mu\text{m V}^{-1} \text{s}^{-1}$) | Mean scattering cross-section σ_{scat} (nm^2) | Laser Power P (mW) | Time Step Δt (μs) | Microfluidic Height h (nm) |
|--------------------|--|--|----------------------|--|------------------------------|
| 100 nm polystyrene | 20 | 36 | 20 | 3.75 | 690 |
| 130 nm polystyrene | 20 | 120 | 7 | 3.75 | 690 |
| 80 nm polystyrene | 30 | 7 | 20 | 3.75 | 690 |
| 50 nm gold | 40 | 52 | 7 | 3.75 | 690 |
| Carboxysomes | 20 | 2 | 20 | 18.75 | 1260 |

Supplementary Figures

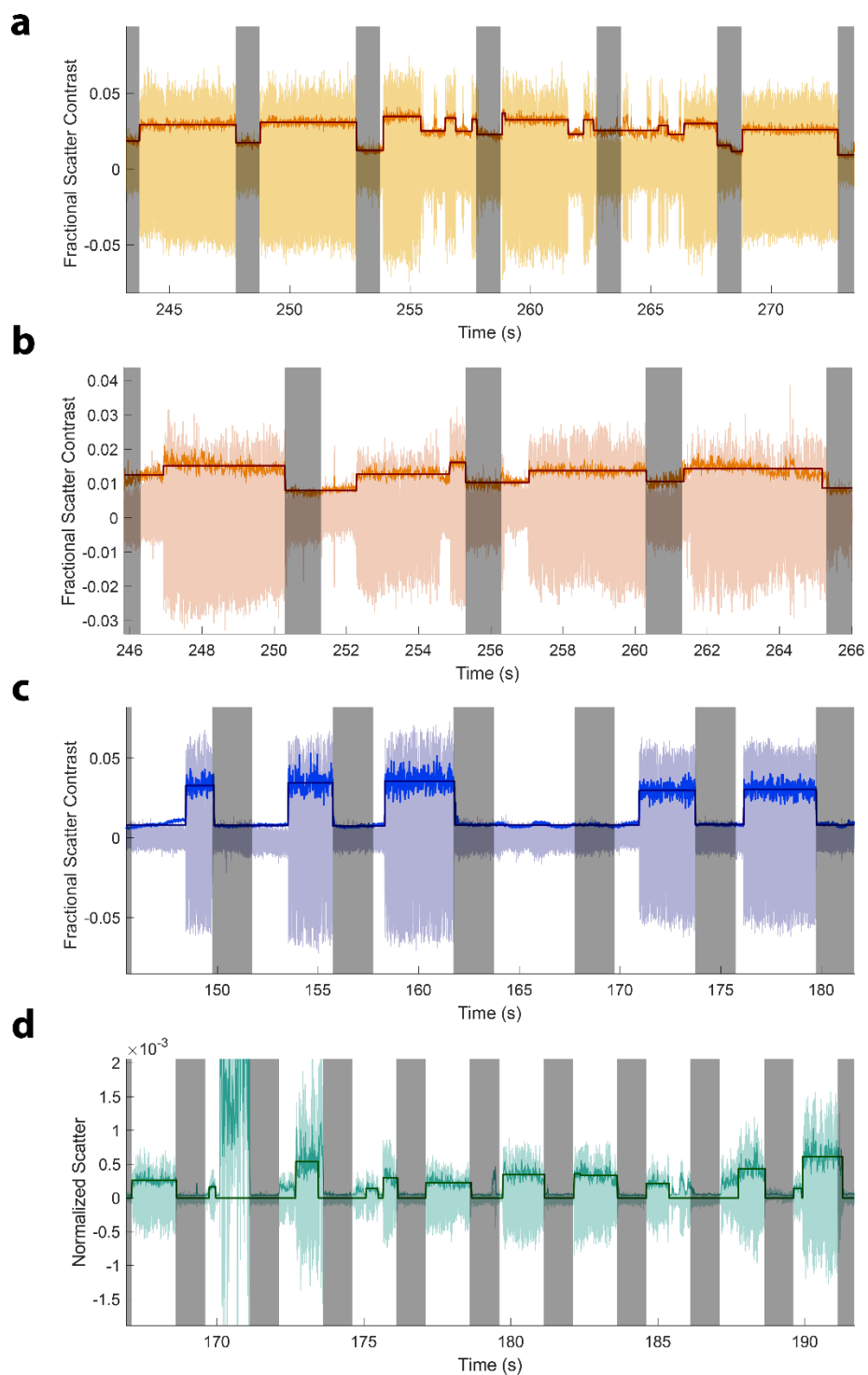


Figure S1: Sample trapping trajectories from additional nanoparticles: (a) 50 nm Au beads, (b) 80 nm polystyrene beads, (c) 130 nm polystyrene beads, and (d) carboxysomes.

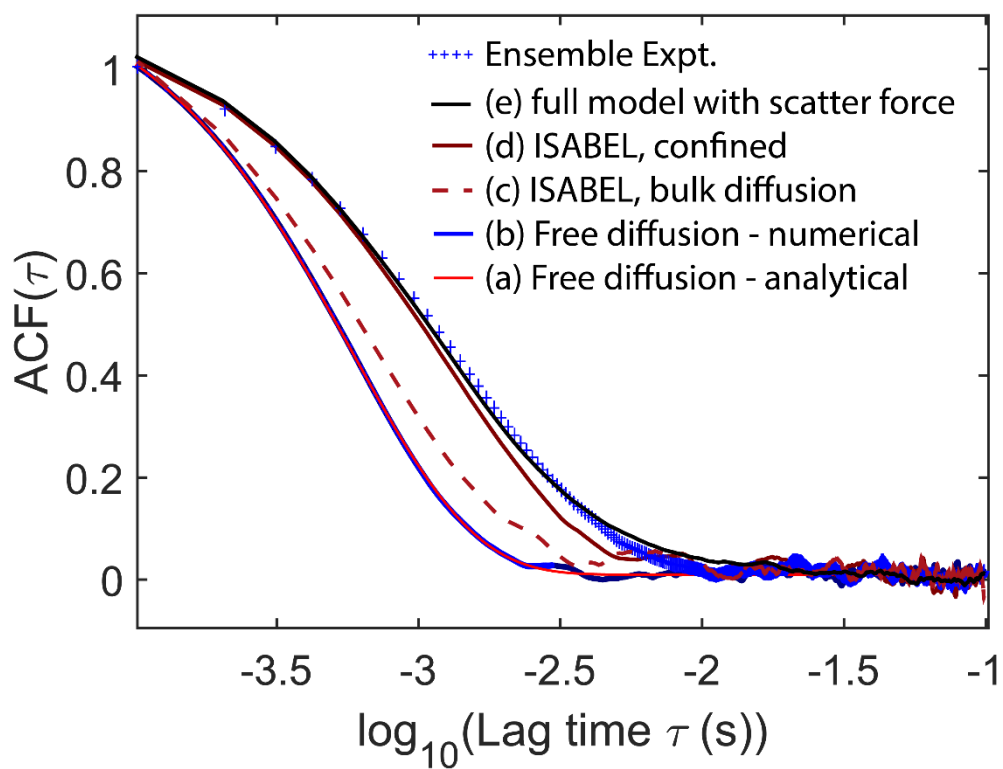


Figure S2: ACF curves for free diffusion of a 110 nm bead versus contributions to the ISABEL experiment. (a) Analytical free diffusion in one dimension (b) numerical model, (c) contrast ACF in the ISABEL trap for a particle subject to an isotropic diffusion coefficient (no confinement), (d) ISABEL trap with confinement effects, and (e) full model, including optical scattering forces.

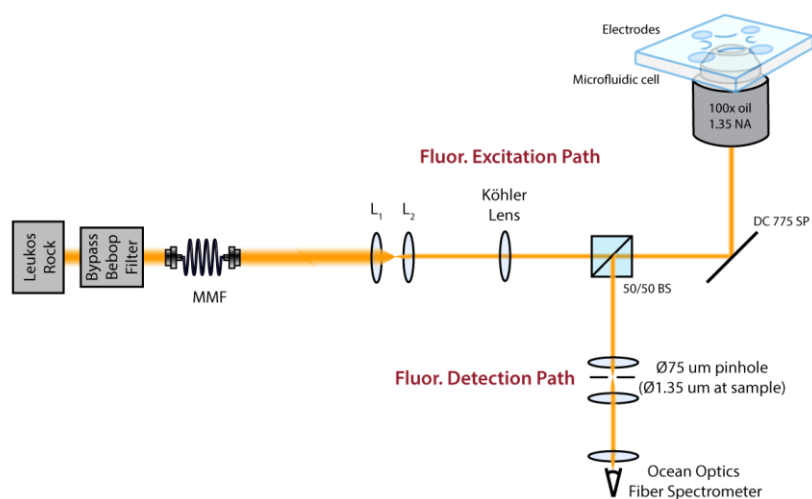


Figure S3: White-light illumination path to determine the ABEL microfluidic height h .

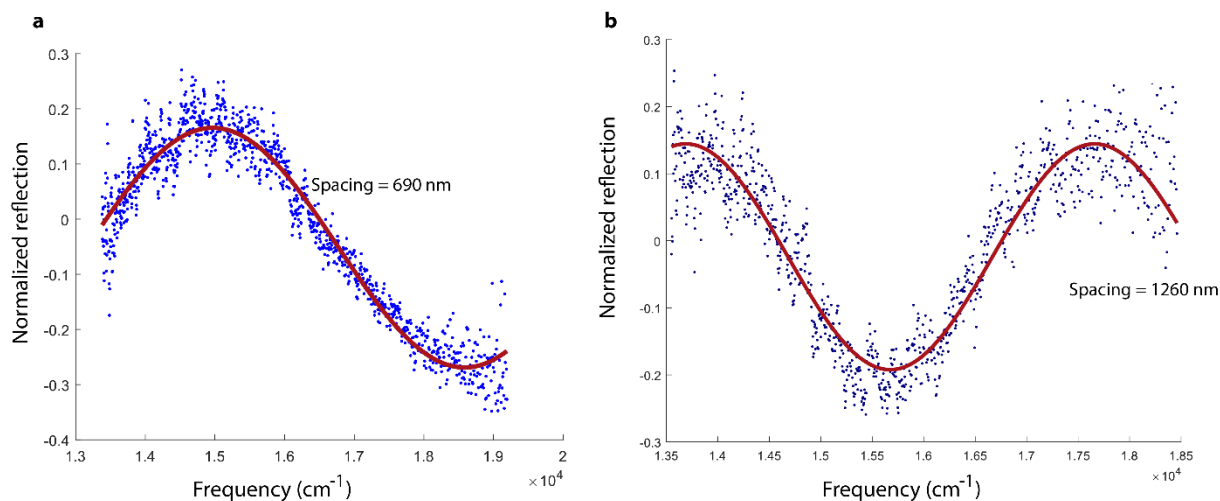


Figure S4: Normalized reflected interference and sinusoidal fit as a function of optical frequency. (a) Reflectivity in the microfluidic cell used for bead standards. (b) Reflectivity for the microfluidic cell used to trap carboxysomes.

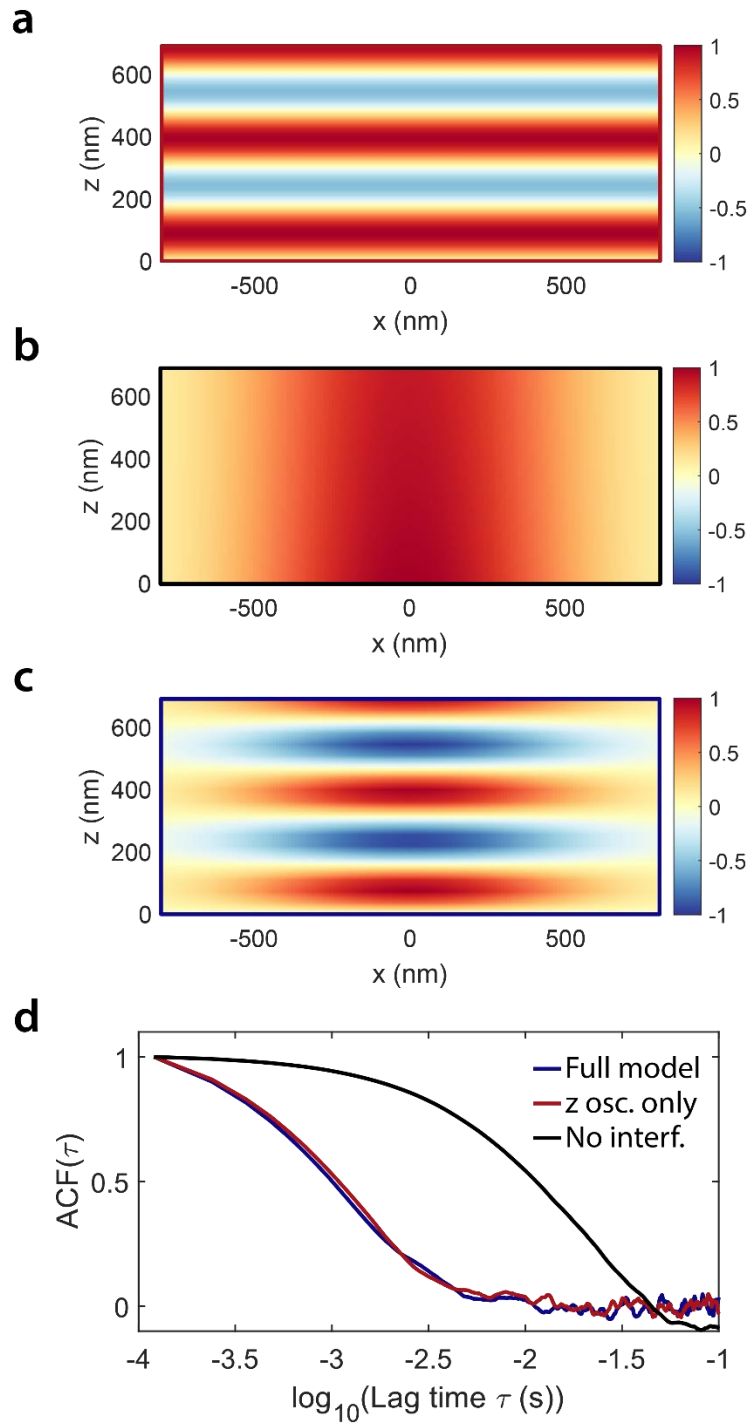


Figure S5: Assessment of the lateral vs axial diffusion components in the contrast ACF. (a) Contrast map with only interference, generated by removing the Gaussian beam waist contributions in Eq. S13 and S14. (b) Contrast map without interference effects. (c) Full contrast model. (d) Simulated ACFs for a trapped 110 nm bead under each contrast model.

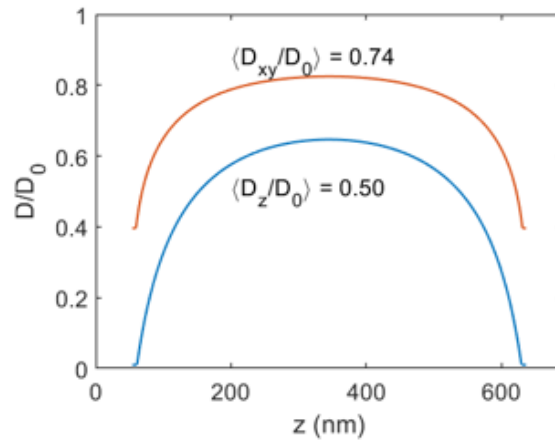


Figure S6: The diffusion attenuation experienced by a $d_H = 100$ nm particle between two walls separated a distance $h = 690$ nm. The orange curve corresponds to lateral diffusion with the average attenuation shown in brackets, while the blue curve shows axial diffusion. Diffusion attenuation is strongest near the walls, and the axial motion is more heavily attenuated by the presence of two walls.

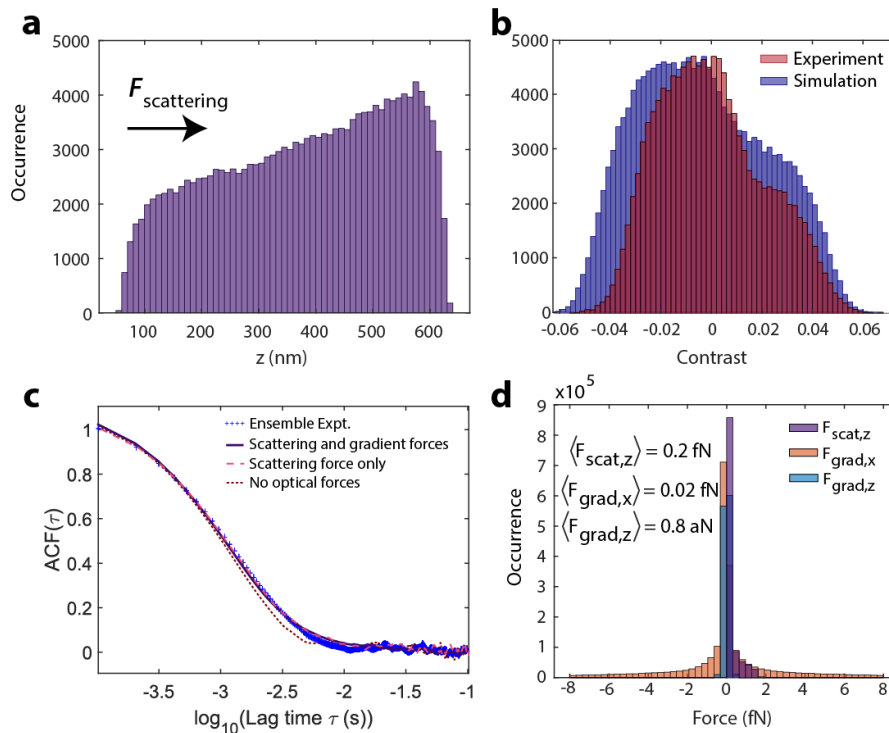


Figure S7: Influence on optical scattering on (a) distribution of z positions of a 110nm polystyrene particle and (b) on asymmetry of the contrast histogram. (c) ACFs with various contributions of optical forces. Simulations with the scattering force only (and gradient forces turned off) match the full model. (d) Distributions of instantaneous forces demonstrate that the scattering force is always positive, whereas the gradients forces evenly samples positive and negative values, leading to a smaller average value.

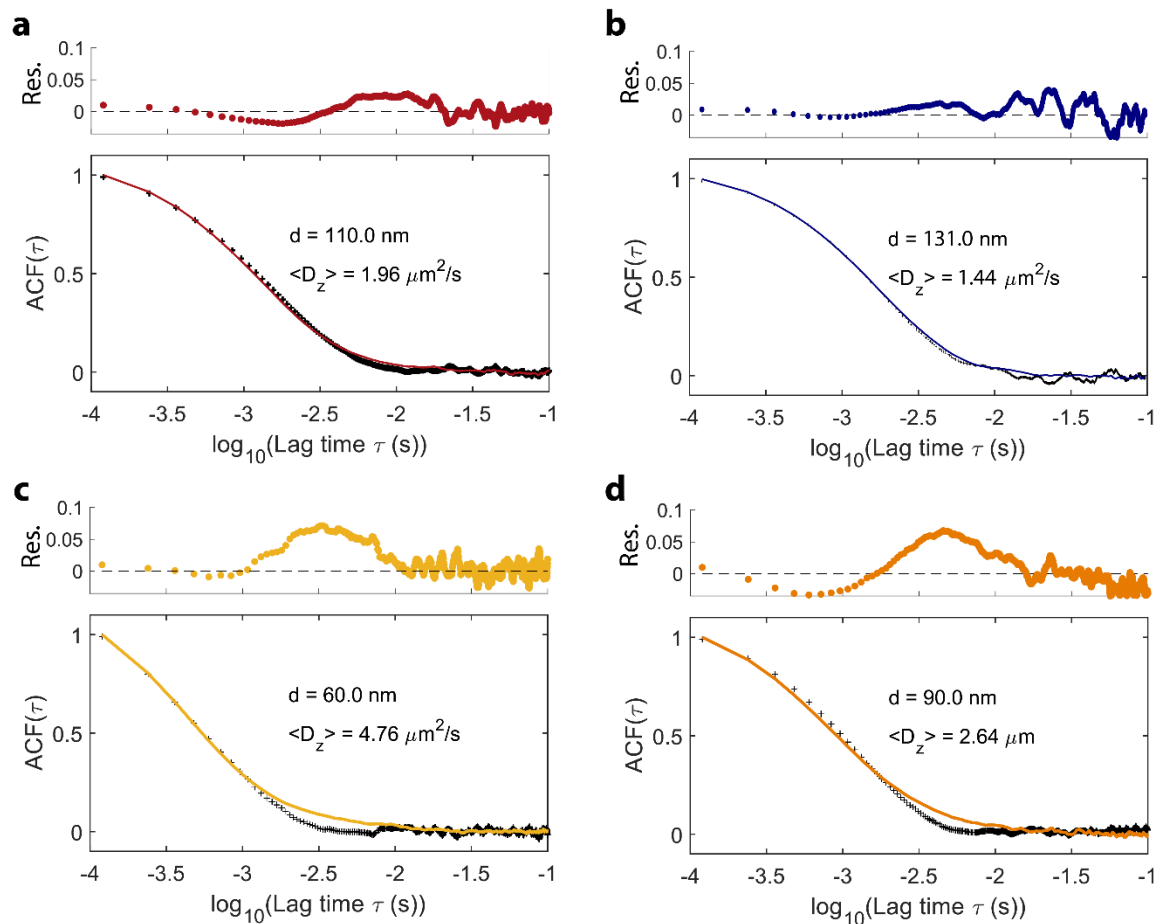


Figure S8: Comparison between numerical simulations of standard bead contrast ACFs with 10-bead ensemble-averaged measured ACFs: (a) 100 nm polystyrene beads, (b) 130 nm polystyrene beads, (c) 50 nm gold beads, and (d) 80-nm polystyrene beads. We note that the curves are not fits to experimental data, but generated from simulations with parameters listed in Tables S1 and S2.

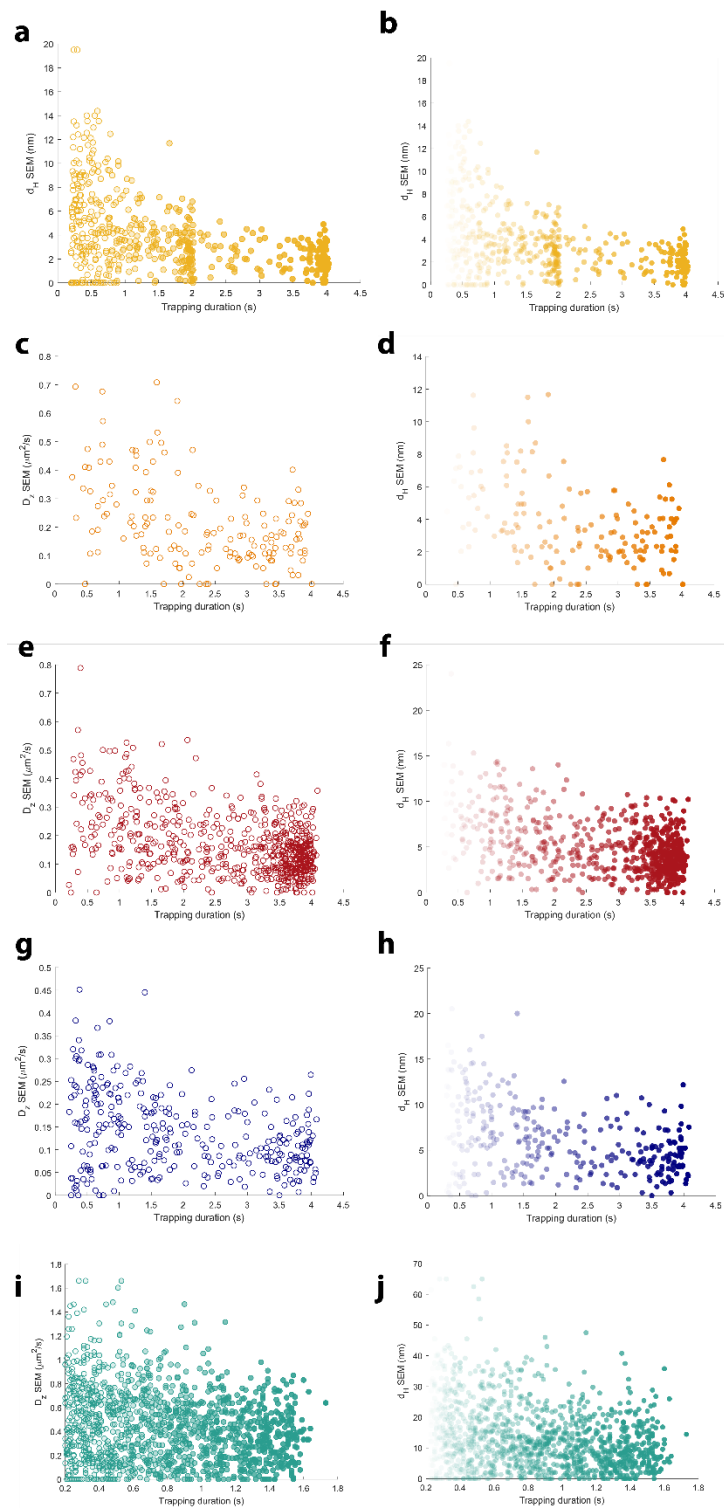


Figure S9: Standard errors of the mean (SEMs) for $\langle D_z \rangle$ (left column) and d_H (right column) estimates for all particles trapped. (a)-(b) 50 nm Au beads, (c)-(d) 80 nm polystyrene, (e)-(f) 100 nm polystyrene, (g)-(h) 130 nm beads, and (i)-(j) carboxysomes.

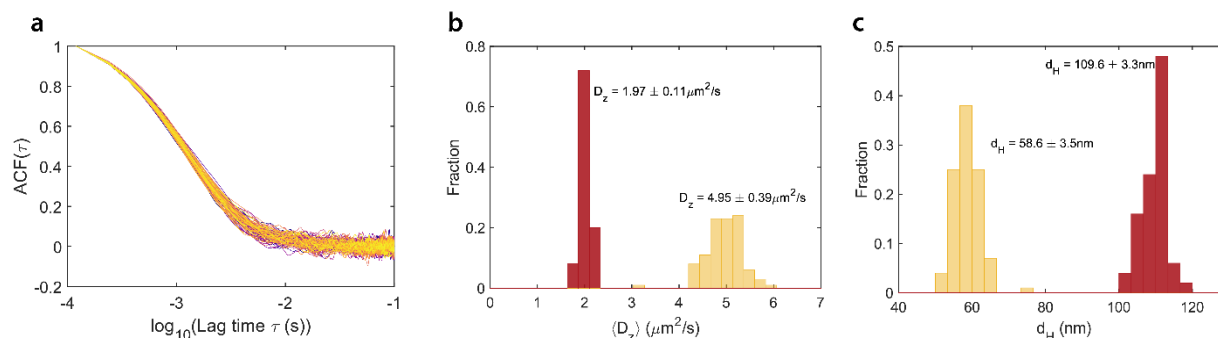


Figure S10: Benchmarking ACF fitting precision and accuracy with 100 identical model particles of fixed d_H for 110 nm polystyrene particles and 59 nm Au particles. Simulations were conducted for 4s trapping events and recorded without experimental noise. (a) ACFs from 110nm beads, demonstrating variation in the ACF decay time due to finite statistical sampling over the trapping interval. (b) D_z results and (c) d_H results.

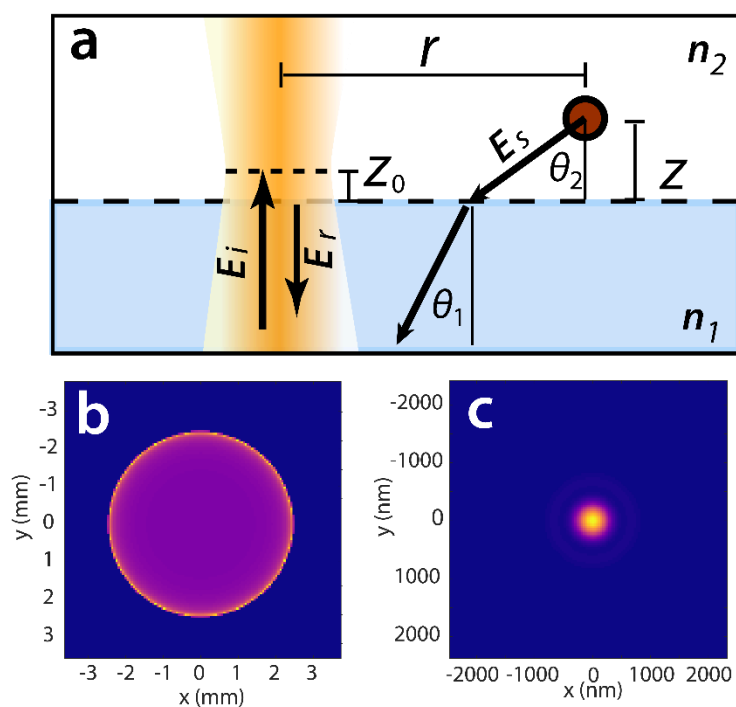


Figure S11: (a) Coordinate system and sample electric field calculations in the (b) back focal plane (magnification 100x) and (c) effective image plane used for the contrast model, plotting the intensity of the scatterer PSF. In (a), the polar angle ϕ of the dipole emission is not shown, and the beam-particle distance r is not to scale.

Supplementary References

- 1 X. Bian, C. Kim and G. E. Karniadakis, *Soft Matter*, 2016, **12**, 6331–6346.
- 2 B. Lin, J. Yu and S. A. Rice, *Phys. Rev. E*, 2000, **62**, 3909–3919.
- 3 A. A. Lavania, W. B. Carpenter, L. M. Oltrogge, D. Perez, J. B. Turnšek, D. F. Savage and W. E. Moerner, *J. Phys. Chem. B*, 2022, **126**, 8747–8759.
- 4 G. Pesce, P. H. Jones, O. M. Maragò and G. Volpe, *Eur. Phys. J. Plus*, 2020, **135**, 949.
- 5 R. W. Taylor and V. Sandoghdar, *Nano Lett.*, 2019, **19**, 4827–4835.
- 6 M. A. Lieb, J. M. Zavislan and L. Novotny, *J. Opt. Soc. Am. B*, 2004, **21**, 1210–1215.
- 7 A. S. Backer and W. E. Moerner, *J. Phys. Chem. B*, 2014, **118**, 8313–8329.
- 8 D. Axelrod, *J. Microsc.*, 2012, **247**, 147–160.
- 9 H. D. Jenkins and Y. Marcus, *Chem. Rev.*, 1995, **95**, 2695–2724.